Nonlinearity-Aware ZUPT-Aided Pedestrian Inertial Navigation Based on Cubature Kalman Filter in Urban Canyons

Ruijie Xu⬭, Shichao Chen⬭, *Member, IEEE*, Shiyu Bai⬭, *Member, IEEE*, and Weisong Wen⬭, *Member, IEEE*

Abstract— Urban pedestrian navigation is a challenging issue as the most popular positioning source, global navigation satellite systems (GNSSs), is severely affected by signal reflections or blockages from high-rise buildings. Unlike the GNSS, the inertial measurement unit (IMU) is less sensitive to environmental conditions but is, unfortunately, subject to drift over time. Applying the motion constraints, such as the zero-velocity update (ZUPT), is a promising solution for mitigating the drift. However, existing zero-velocity (ZV) detections can cause false results in urban scenarios involving more complex pedestrian motions. Meanwhile, the IMU-based model's nonlinearity further reduces the accuracy of the state estimation. This article proposes a nonlinearity-aware ZUPT-aided pedestrian inertial navigation in urban canyons to fill this gap. Our method begins with a gait interval (GI)-aided dual-threshold ZV detection scheme to prevent false or missed detections in complex pedestrian motions. A ZUPT-aided inertial navigation based on cubature Kalman filter (CKF) is formed to mitigate the impact of nonlinearity. Several datasets are collected to validate the effectiveness of the proposed method. The experimental results demonstrate that the proposed method can detect ZV more accurately and estimate pedestrian location more precisely with the CKF than extended Kalman filter (EKF) and unscented Kalman filter (UKF)-based methods. Meanwhile, the time consumption of the proposed method is essentially on par with the UKF-based method. It achieves a balance between computational efficiency and accuracy, which provides a low-drift self-contained real-time inertial navigation for pedestrians when external positioning data are unavailable. To benefit the research community, we open-source our dataset via GitHub: https://github.com/RuijieXu0408/PINS-datasets-based-on-Xsens-IMU.

Index Terms— Cubature Kalman filter (CKF), inertial sensor, nonlinearity, pedestrian navigation, zero-velocity (ZV) detection.

Nomenclature

c_k	Pedestrian's motion state.
$\mathbf{a}_k^n$	Acceleration in navigation frame.
G	Gravity.
$\mathbf{v}_k^n$	Pedestrian's velocity.
$\mathbf{C}_{b,k}^n$	Rotation matrix from body frame to navigation coordinate.
$\boldsymbol{\chi}_{k|k-1}^i$	State equation with cubature point.
$\hat{\mathbf{X}}_k$	Estimated pedestrian's state equation.
$\mathbf{Z}_k^i$	Cubature point set for calculating measurement model.
$\mathbf{R}_k$	Covariance of ZUPT measurement noise.
γ	Thresholds for ZV detection.
$\boldsymbol{\omega}_k^b$	Angular rate in body frame.
$\mathbf{x}_k$	Pedestrian's gait system.
$\mathbf{p}_k^n$	Pedestrian's position.
$\mathbf{P_k}$	Covariance matrix of state equation.
$\mathbf{Q}_k$	Process covariance.
$\mathbf{Y}_k^i$	Measurement model based on cubature point.
$\mathbf{K}_k$	Kalman gain.

I. Introduction

THE inertial-based pedestrian positioning is highly expected in global navigation satellite system (GNSS)-challenged scenarios; GNSSs with highly accurate 3-D positioning capability are now widely used in pedestrian navigation [1], [2]. To compensate for errors within the GNSS system, real-time kinematic (RTK) technology has been proposed to enable more accurate outdoor positioning [3], [4]. Unfortunately, the performance of the GNSS is significantly degraded in urban canyons due to the severe signal reflections and blockages from the surrounding high-rise buildings, leading to the notorious multipath effects and the non-line-of-sight (NLOS) receptions [5], [6]. An inertial navigation system (INS) is typically employed to obtain navigation parameters without external reference. It is self-contained and has been widely integrated into various devices in recent years to compensate for the GNSS positioning inaccuracy in interior or heavily occluded outdoor environments [7], [8]. There are two main categories of INSs: stable platform-based and strapdown INSs (SINSs) [9]. Unlike the former, SINS embeds inertial sensors directly onto the carrier without a platform to estimate the user's position. This significantly reduces its size and weight. Besides, with the rapid development of micro-electromechanical system (MEMS) technology, small and portable inertial measurement units (IMUs) have been extensively used by pedestrians for self-positioning. However, SINS based on MEMS IMU is prone to rapid drift due to the high sensor noise [10]. Therefore, researchers have employed human motion characteristics to reduce SINS errors.

Zero-velocity update (ZUPT) can help but is challenged in urban scenes with complex pedestrian motion. There are two main motion-based methods for mitigating the drift of SINS

over time: pedestrian dead reckoning (PDR) [11] and ZUPT-aided [pedestrian INS (PINS)] [12]. Both of these approaches are based on IMU for position estimation. However, the PDR algorithm is subject to user variation, dependent on human height, leg length, and step frequency. ZUPT is mainly used for foot-mounted IMU, which is less affected by individual user variation and the external environment and has gained many researchers' attention. Skog et al. [13] proposed an open-source, real-time foot-mounted ZUPT-aided PINS. In addition, they studied the influence of error models on foot-mounted INSs and then published a locally distributed system framework. Unfortunately, commonly used zero-velocity (ZV) detections of ZUPT, including the generalized likelihood ratio test (GLRT) detector [14] and acceleration magnitude (MAG) detector [15], still have the issue of misjudging the pedestrian's gait interval (GI) when complex motions are involved, which leads to some errors in positioning.

The nonlinearity of the SINS model challenges the estimators, Unlike vehicle positioning, which generally moves along the road and has a slow change in velocity, the moving velocity and heading of pedestrians are more random. In addition, pedestrians' orientations are more variable, such as swaying back and forth and turning around. When the IMU is mounted to a pedestrian's foot, the IMU is also subjected to the impact caused by the foot touching the ground. As a result, the nonlinear characteristic of the SINS model is another critical challenge in addition to the cumulative error. The detailed description of the nonlinearity analysis is introduced in Section III. Therefore, a rising accuracy requirement for a state estimator for ZUPT-aided PINS exists. To face these challenges, Kalman filter (KF)-based methods are usually introduced in ZUPT-aided PINS, with the extended KF (EKF) and unscented KF (UKF) being the most widely used [16]. However, a first-order Taylor expansion step that the EKF algorithm relies on will cause larger errors and lower estimation accuracy. Meanwhile, the sigma point used for nonlinear approximation in UKF has some parameters that need to be set appropriately, such as the tuning parameter κ, which will be introduced in the estimator part of [17, Sec. II]. This point is very important and requires more weights, usually negative for higher dimensional systems. As explained by Zarei and Shokri [17], nonpositive weights lead to interruptions in the prediction iterations.

To sum up, the primary challenges addressed in this work are insufficiently accurate ZV detection methods, nonlinear characteristics of the SINS model, and cumulative errors from IMU calculations. Based on the above problems, we propose a novel nonlinearity-aware pedestrian inertial navigation based on GI-aided ZUPT and cubature KF (CKF). To the best of our knowledge, this approach is the first discussion to explore the use of CKF to suppress the error of nonlinearity in ZUPT-aided pedestrian inertial navigation. In addition, the additional novelty of this approach is developing a GI-aided dual-threshold ZV detection method to identify pedestrian GIs in a lightweight and efficient manner, and it can improve the accuracy rate and reliability of ZV detection. The flowchart is given in Fig. 1. The main contributions of this article are listed as follows.

1) *A GI-Aided Dual-Threshold ZV Detection:* Lightweight dual-threshold ZV detection, consisting of an acceleration variance detector and angular rate energy (ARE) detector, is proposed to detect the ZV during pedestrian movement accurately. Besides, due to the alternating motion-stationary-motion gait of a person while walking, we fit the pedestrian intervals detected by dual thresholds to remove the erroneously detected outliers during the walking process, thereby improving the accuracy rate of the ZV detection.

2) *CKF-Based SINS/ZUPT Integration:* To ensure the real-time performance of the system, a novel ZUPT-aided PINS based on CKF is formed, effectively suppressing the influence of nonlinear errors brought by EKF and the iteration failure brought by the setting of the UKF sigma point, leading to a more accurate estimation of the pedestrian's motion state than existing methods.

3) *Extensive Experimental Validation:* The performance of the proposed method in ZV detection and trajectory estimation is evaluated via comparative experiments. The results show that the proposed method performs well in different scenarios. To benefit the research community, our PINS dataset is open-sourced and is available on GitHub [18].

The rest of this article is organized as follows. Related works are presented in Section II, which is followed by a detailed description of the proposed methodology in Section III. The real-scenario experiments and the discussion of the proposed method are elaborated in Section IV. Finally, the conclusions are drawn in Section V.

II. RELATED WORKS

Since PDR and ZUPT methods use the same information acquisition equipment and data type, many approaches [19] classified the ZUPT-aided PINS into PDR. In order to better describe the solving process of these two methods, we separately describe the PDR and ZUPT.

A. Motion Constraint-Aided Pedestrian Positioning

The PDR consists of step detection, step length, and heading estimation [20]. For example in Fig. 2(a), we can use the pedestrian's position at the previous moment $\mathbf{p}_0, \mathbf{p}_1, \ldots, \mathbf{p}_{k-1}$, the estimated pedestrian's heading $\theta_1, \theta_2, \ldots, \theta_k$, and the estimated pedestrian's step length $d_1, d_2, \ldots, d_k$ to calculate the current position $\mathbf{p}_1, \mathbf{p}_2, \ldots, \mathbf{p}_k$.

SmartPDR, proposed by Kang and Han [21], successfully tracked indoor users' location, and Beauregard and Klepal [22] used minimal map information and particle filters to introduce indoor PDR performance enhancement. However, these PDR methods focus on 2-D coordinates such as north–east coordinates. Ji et al. [23] also mentioned that PDR does not work well in up-and-down scenarios. In addition, the PDR algorithm is subject to user variation, which is dependent on human parameters, such as height, leg length, and step frequency, and the variation between individuals can greatly affect the applicability of the algorithm model. In contrast, Zhao and Ahamed [24] mentioned that the ZUPT mechanism
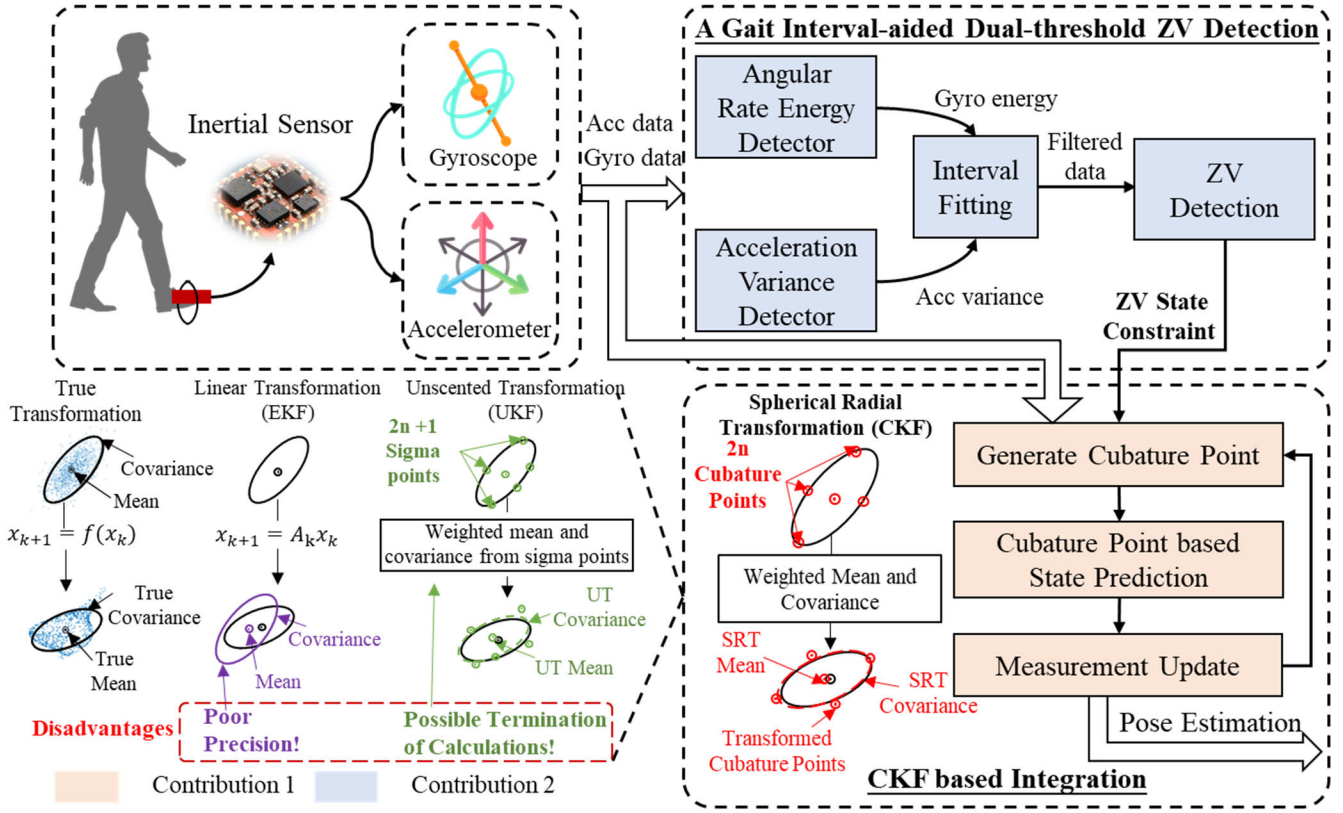
Fig. 1. Flowchart of the proposed nonlinearity-aware pedestrian inertial navigation based on GI-aided ZUPT and CKF.
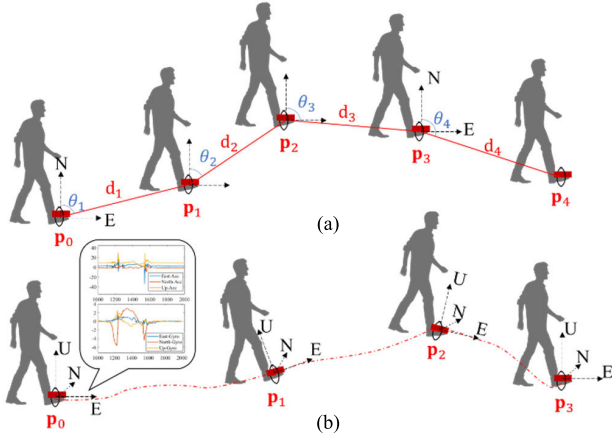

Fig. 2. Comparison of the IMU-based pedestrian positioning method. (a) PDR algorithm and (b) ZUPT-aided PINS.

is less affected by individual user variation and the external environment and has gained the attention of many researchers.

ZUPT was introduced into geodesy in the 1970s for surveys using accurate stand-alone INS [25], [26]. The system would stay at a well-defined position for several minutes to perform INS updates. In 2005, Foxlin [27] first introduced ZUPT to aid pedestrian inertial navigation. ZUPT-aided PINS mainly relies on the measured ZV during the pedestrian's stationary phase to correct the cumulative error generated by IMU, thus improving positioning accuracy, as shown in Fig. 2(b). To be specific, the pedestrian's orientation $\mathbf{S}_1, \mathbf{S}_2, \ldots, \mathbf{S}_k$ are first predicted via the previous moment's orientation $\mathbf{S}_0, \mathbf{S}_1, \ldots, \mathbf{S}_{k-1}$ and IMU outputs. ZV is utilized as an observation in an estimator to achieve the update.

B. ZV Detection

The purpose of detecting the ZV state of pedestrians is to use the observation to suppress the positioning error. Many kinds of ZV detection approaches are based on predefined thresholds [28], and their performance depends on pedestrian movement patterns and threshold settings. Predefined thresholds are most widely used in the field of ZV detection, which includes the widely known MAG detector, the acceleration moving variance (MV) detector, and the ARE detector proposed by Skog et al. [14]. They are characterized by the amplitude of the current acceleration, the covariance of the acceleration, and the angular velocity energy of the pedestrian to determine the current motion state. Although these detection methods are lightweight, according to Li et al. [29], these methods still have many false and missed detections.

As a hypothesis testing method, the GLRT detector is another fixed threshold detector widely used by scholars [23]. The basic idea of GLRT is to calculate the maximum likelihood ratio under two hypotheses for given data and then compare this ratio with a threshold. If the ratio exceeds the threshold, one of the hypotheses should be accepted. Otherwise, the other hypothesis should be accepted. In ZV detection, the two assumptions are usually the presence of ZV and non-ZV. The advantage of GLRT is that it does not need to know the exact parameter value, only the possible range. However, the limitation of GLRT is that it loses the advantage of being lightweight compared with other fixed threshold detectors. In addition, it still requires setting a possible threshold.

Meanwhile, another detection method, i.e., Cho and Park [30], denoted that ZV is detected by recognizing the

shapes of simplified signals of angular rate and acceleration. With the rapid development of deep learning techniques, some researchers have attempted to perform ZV detection using CNN [31] and LSTM [32] to solve the problem of manually setting thresholds in the above techniques. In addition, some studies have introduced additional sensors to assist ZV detection, such as radio frequency identification (RFID) [33], ultrawideband (UWB) [34], dual-IMU [35], and ultrasonic ranging [36]. Indeed, learning-based ZV detections or introducing additional ones can detect pedestrians' ZV more accurately. However, these methods require additional equipment, and the power consumption and computational cost increase tremendously, making it challenging to deploy in portable INSs.

C. Estimator for the Pedestrian Positioning

Optimal filter has been widely used to integrate ZUPT with inertial navigation. A typical representative of optimal filtering in navigation is the KF [37]. However, classical KF can only handle linear systems. Given the nonlinearity in the inertial navigation model, nonlinear filtering-based methods derived from KF need to be employed.

EKF is the most commonly used nonlinear filtering algorithm in real-time pose estimation. Foxlin [27] first introduced EKF to fusion the data from shoe-mounted inertial sensors, providing a lightweight PINS solution. Zhang et al. [38] designed a Bayesian ZV detection algorithm based on threshold judgment to transform the carrier and pedestrian geographic coordinate system to effectively recognize posture and accurately count steps. However, the precision of these approaches is limited by the accuracy of EKF. When the degree of nonlinearity of the system becomes stronger and it is difficult to fit it into a linear state, the first-order Taylor series expansion step that the EKF algorithm relies on will produce larger errors and lead to low estimation accuracy or even divergence of the filter.

UKF is an algorithm developed by Julier and Uhlmann [39] that aims to avoid the linearization required by EKF. UKF employs unscented transformation to estimate the mean and covariance of a random variable that is subjected to a nonlinear transformation. Instead of directly computing the posterior mean and covariance of the state vector, unscented transformation approximates these statistics using a carefully selected set of points known as *sigma points*. These *sigma points* are deterministically chosen to achieve at least second-order accuracy in the estimation process without needing tedious analytical linearization such as EKF [40]. The prior statistics of the state vector are then obtained by propagating the selected *sigma points* through the nonlinear function, allowing the UKF to capture the effects of the nonlinearity on the state estimation. Hajati and Rezaeizadeh [41] proposed a UKF-based wearable pedestrian localization. However, according to Garcia et al. [42], the limitations of UKF come from the deterioration of computational efficiency. Furthermore, as mentioned by Zarei and Shokri [17], the sigma points in UKF have tuning parameters that require appropriate settings. The key concern lies in the additional center point with the tuning parameter κ

in UKF. For parameter estimation, κ is usually set to $3 - n$, where n is the dimension of the state vector. The choice of κ affects the weight assigned to the central sigma point, which is given by $W = \kappa/(n + \kappa)$. When the system dimension is greater than 3 ($n > 3$), the negative weight of the center sigma point can cause the calculated covariance to become nonpositive semi-definite, interrupting the iterative process. Therefore, the UKF algorithm has difficulties in dealing with high-dimensional problems.

CKF was proposed by Arasaratnam and Haykin [43] as an alternative estimation algorithm for the general nonlinear system. Based on the spherical–radial cubature rule, it is the closest theoretical approximation to Bayesian filtering. It is a powerful third-order accuracy tool for solving state estimation of nonlinear systems. Compared with UKF, the cubature points are fixed in CKF, which will not cause the iterative interrupt in UKF. It performs better than the EKF and UKF regarding estimation accuracy, numerical stability, and computational cost in higher order nonlinear states [44]. There are some implementations in other state estimation areas, such as power systems [45] and dynamic harmonic estimation [46], while there are few applications in PINS fields.

In pedestrian INS, the pedestrian walking position is discrete and unpredictable due to the fast change of direction and velocity when the pedestrian walks, especially in urban canyons. Therefore, solving the pedestrian state equation has strong nonlinear characteristics. In addition, the state dimension of the INS is relatively high. Considering the drawbacks of using EKF and UKF, this article considers CKF an alternative and more competitive filter for the ZUPT-aided pedestrian INS.

III. METHODOLOGY

The working principle of the PINS is given as follows. Data are collected by a foot-mounted IMU and used for state prediction and ZV detection. An error correction algorithm updates the position, velocity, and attitude. Moreover, before introducing these two parts, we should first illustrate the gait cycle and which parts are regarded as stationary. We put the significant symbols in Nomenclature for easy checking. Besides, the body frame and its three-axis are represented as b and x, y, z, respectively, and the earth–north–up coordinate and its three-axis are represented as n and E, N, U.

A. Pedestrian's Gait Cycle

The pedestrian's gait cycle is necessary to study the ZUPT algorithm [47]. We usually refer to the process of a pedestrian walking with one toe off the ground to the same foot's toe on the ground as a complete pedestrian gait cycle [41]. Its four phases, including stance, propulsive, swing, and grounding phases, are shown in Fig. 3. We can consider the phase of the pedestrian gait cycle in which the toes touch the ground as the stationary state. Numerous studies have sought to investigate the effect of the location of the mounted IMU on the pedestrian to the effect of ZV detection [48]. Experiments have indicated that foot-mounted mounting maximizes the capture of pedestrian motion.
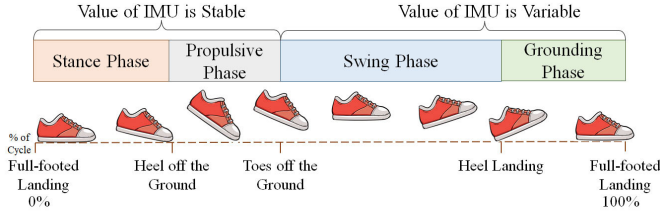
Fig. 3. Complete cycle of pedestrian gait.

The nonlinear characteristics of the SINS derive from the uncertainty of pedestrian gait compared to vehicular motion and the process of calculating pedestrian position. First, inertial positioning is a relative positioning technique, its state prediction performance at that moment is highly dependent on the prediction result of the previous moment, and pedestrians often have changes in direction and speed during walking compared to vehicle motion. Meanwhile, the accelerometers and gyroscopes in the foot-mounted IMU change too fast during the pedestrian's foot-lifting process, and the sampled data will generate some measurement errors. In addition, the position and velocity updates use discrete-time integration of accelerations and velocities. It can introduce errors if the acceleration between two time steps is not constant. The quaternion update assumes small angular changes. For larger angular velocities or longer time steps, the approximation can lead to significant errors in orientation estimation. While the calculation method described is a common approach in pedestrian inertial navigation, it is subject to nonlinear errors due to the reasons discussed above. Understanding and mitigating these errors is crucial for improving the accuracy and reliability of the navigation system.

In ZUPT-aided PINS, we need to measure the pedestrian's ZV to trigger the correction. Trupti Gujarathi's Experiments have demonstrated that the measured values of the IMU differ significantly during the stance and propulsive phases from the swing and grounding phases [49]. During the stance and propulsive phase, the IMU measurements of the pedestrian are essentially stable: the foot-mounted gyroscope and horizontal accelerometer values are around zero, and the vertical accelerometer values are around gravitational. In contrast, the accelerometer and angular gyroscope values vary considerably during the swing and grounding phases. Using IMU values as observables, we can divide the four phases of the pedestrian's gait cycle into both states: the stance and propulsive phases are considered the ZV state, and the swing and grounding phases are considered the motion state.

B. GI-Aided Dual-Threshold ZV Detection

The ZV detection algorithm is essential to the inertial navigation error correction. The ZV and motion phases in the walking gait can be differentiated using periodic dynamic changes captured by the three-axis accelerometer and three-axis gyroscope in the IMU. The mathematical model for dual-threshold ZV detection can be viewed as a problem of hypothesis testing, where ZV detection is a binary hypothesis. We refer to the result of ZV detection of pedestrian gait at moment k as c_k. Also, k denotes a time instant during the

travel of the pedestrian. During the moment k, if the pedestrian is at the ZV state, c_k is 0. On the contrary, when the pedestrian is in motion, c_k is 1, which can be expressed as

$$c_k = \begin{cases} 0, & T_1 < \gamma_1 \text{ and } T_2 < \gamma_2 \\ 1, & \text{otherwise} \end{cases} \quad (1)$$

where T_i represents the transformation related to acceleration and angular rate in the body frame during the pedestrian's movement. T_1 can be represented as

$$T_1 = \sqrt{\sigma(a)_{x,k}^{b}{}^2 + \sigma(a)_{y,k}^{b}{}^2 + \sigma(a)_{z,k}^{b}{}^2} \quad (2)$$

where $\sigma(a)_{x,k}^b$, $\sigma(a)_{y,k}^b$, and $\sigma(a)_{z,k}^b$ represent the variance of acceleration measured by IMU. They can be calculated as

$$\sigma(a)_{x,k}^b = \sqrt{\frac{\sum_{i=k-m}^{k+m}\left(\mathbf{a}_{x,i}^b - \bar{\mathbf{a}}_{x,k}^b\right)^2}{2m+1}} \quad (3)$$

$$\sigma(a)_{y,k}^b = \sqrt{\frac{\sum_{i=k-m}^{k+m}\left(\mathbf{a}_{y,i}^b - \bar{\mathbf{a}}_{y,k}^b\right)^2}{2m+1}} \quad (4)$$

$$\sigma(a)_{z,k}^b = \sqrt{\frac{\sum_{i=k-m}^{k+m}\left(\mathbf{a}_{z,i}^b - \bar{\mathbf{a}}_{z,k}^b\right)^2}{2m+1}} \quad (5)$$

where $\mathbf{a}_{x,i}^b$, $\mathbf{a}_{y,i}^b$, and $\mathbf{a}_{z,i}^b$ are the acceleration at moment i measured in the body frame x-, y-, and z-directions, respectively. Moreover, $\bar{\mathbf{a}}_{x,k}^b$, $\bar{\mathbf{a}}_{y,k}^b$, and $\bar{\mathbf{a}}_{z,k}^b$ are the mean acceleration over the sliding window centered at moment k measured in the body frame x-, y-, and z-directions, respectively.

When a pedestrian's foot touches the ground, the output vectors of three-axis gyroscopes ω_x^b, ω_y^b, and ω_z^b are more stable than the accelerations. Therefore, the MAG of the pedestrian's angular rate can be another observation to measure the state of the pedestrian, which is expressed as

$$T_2 = \sqrt{\omega_{x,k}^{b}{}^2 + \omega_{y,k}^{b}{}^2 + \omega_{z,k}^{b}{}^2}. \quad (6)$$

γ_1 and γ_2 are the thresholds for ZV detection. Only when T_1 and T_2 meet the threshold constraints simultaneously, can the pedestrian's current state be considered stationary. The thresholds depend on the pedestrian's movement pattern. After data preprocessing and testing, we concluded that during pedestrian walking, the acceleration MV γ_1 within the sliding window of 0.2 s should be less than 0.4 m/s^2 and the amplitude of angular rate γ_2 should be less than 0.4 rad/s.

Data characteristics in T_i can be exploited to recognize the ZV state. For instance, during the movement, the pedestrian's acceleration in the north and east coordinates should be around zero, and the value in the up coordinate should be around gravity. Many detectors, primarily MAG detectors, set a threshold slightly larger than the gravity to evaluate the MAG of a pedestrian's acceleration. However, the amplitude detection method is relatively sensitive to noise and clutter, which may lead to false or missed detection. Especially in complex environments (such as vibrations and bumps), the acceleration of pedestrians changes rapidly, and the amplitudes of noise and clutter may be similar to the motion amplitudes, which may lead to erroneous status judgments. In contrast, the dual-threshold ZV detection we set up can avoid the

problems caused by single detector misjudgment, improving the accuracy rate.

The result of ZV detection may have a few outliers, and in order to eliminate these outliers, we introduce GI-aided detection. During pedestrian walking, the states of the foot at rest and in motion always alternate steadily, and the proportion of the time interval between the two states tends to be constant. Therefore, based on this feature, we can fit the detected pedestrian state c to the interval. After dual-threshold detection, the state of the pedestrian during the whole movement can be represented as follows:

$$\mathbf{c} = \{c_1, c_2, \ldots, c_k, \ldots, c_N\}. \tag{7}$$

Then, we set a smoothing window n around moment k in the data smoothing phase correction. Since the GI of a moving pedestrian should be "static motion" alternately cyclic when the c_k value detected by the detector is inconsistent with more than half of the surrounding $2n$ points, c_k will be corrected, and the expression is given as follows:

$$c_k' = \begin{cases} 0, & c_k = 0 \text{ and } \sum\limits_{j=k-n}^{k+n} c_j \notin (n, 2n) \\ 0, & c_k = 1 \text{ and } \sum\limits_{j=k-n}^{k+n} c_j \in (0, n) \\ 1, & c_k = 1 \text{ and } \sum\limits_{j=k-n}^{k+n} c_j \notin (0, n) \\ 1, & c_k = 0 \text{ and } \sum\limits_{j=k-n}^{k+n} c_j \in (n, 2n). \end{cases} \tag{8}$$

The final interval set can be written as

$$\mathbf{c}' = \{c_1', c_2', \ldots, c_k', \ldots, c_N'\}. \tag{9}$$

Dual-threshold detection provides an efficient and lightweight solution for the ZV detection in the proposed method. The accelerometer and gyroscope data are comprehensively considered for improved detection. In addition, the GI fitting can significantly reduce the problems of misjudgment and false judgment in conventional ZV detection methods.

C. State Prediction Based on Inertial Navigation

In this article, the state vector consists of 10-D variables, including the propagation of pedestrian's attitude, velocity, and position. It can be predicted by the three-axis output value of accelerometers $\mathbf{a}_k^b$ and gyroscopes $\boldsymbol{\omega}_k^b$.

Let the quaternion $\mathbf{q}$ be part of the system state, and the differential equation of the quaternion can be expressed as

$$\dot{q} = \frac{1}{2}\boldsymbol{\Omega}(\boldsymbol{\omega}) \cdot \mathbf{q} \tag{10}$$

where $\mathbf{q} = [q_0, q_1, q_2, q_3]^T$ is the quaternion and $\boldsymbol{\Omega}(\boldsymbol{\omega})$ is the matrix consisting of the angular velocity $\boldsymbol{\omega}_k^b = [\omega_x^b, \omega_y^b, \omega_z^b]^T$

measured by the gyroscope; the matrix can be denoted as

$$\boldsymbol{\Omega}(\boldsymbol{\omega}) = \begin{bmatrix} 0 & -\omega_x^b & -\omega_y^b & -\omega_z^b \\ \omega_x^b & 0 & \omega_z^b & -\omega_y^b \\ \omega_y^b & -\omega_z^b & 0 & \omega_x^b \\ \omega_z^b & \omega_y^b & -\omega_x^b & 0 \end{bmatrix}. \tag{11}$$

Discretize (8) to facilitate iterative calculations as (10)

$$\mathbf{q}_{k+1} = \mathbf{q}_k + \frac{1}{2}(\Delta T) \cdot \boldsymbol{\Omega}(\boldsymbol{\omega}_k^b) \cdot \mathbf{q}_k \tag{12}$$

where $\mathbf{q}_i$ is the pedestrian's quaternion state at moment i and ΔT is the sampling interval of IMU.

The pedestrian's three-axis acceleration in the navigation coordinate denoted by $\mathbf{a}_k^n = [a_E^n, a_N^n, a_U^n]^T$ can be obtained by removing the influence of gravity G as

$$\mathbf{a}_k^n = \mathbf{C}_{b,k}^n \cdot \mathbf{a}_k^b - [0 \quad 0 \quad G]^T \tag{13}$$

where $\mathbf{C}_{b,k}^n$ is the rotation matrix from the body frame b to the navigation frame n at moment k. $\mathbf{a}_k^b$ is the output IMU raw acceleration data in the body frame, so we need to remove the gravity in the vertical direction.

Then, the pedestrian's velocity $\mathbf{v}_{k+1}^n$ and position $\mathbf{p}_{k+1}^n$ at moment $k + 1$ can be updated based on the previous velocity $\mathbf{v}_k^n$ and acceleration $\mathbf{a}_k^n$ at moment k as

$$\mathbf{v}_{k+1}^n = \mathbf{v}_k^n + \mathbf{a}_k^n \cdot \Delta T \tag{14}$$

$$\mathbf{p}_{k+1}^n = \mathbf{p}_k^n + \mathbf{v}_k^n \cdot \Delta T + \frac{1}{2}\mathbf{a}_k^n \cdot \Delta T^2 \tag{15}$$

where ΔT is the time interval between moment k and moment $k + 1$, which is usually determined by the sampling time of IMU.

By combining (12), (14), and (15), we can obtain the predicted state vector of the pedestrian gait system $\mathbf{x}_{k+1}$ at moment $k + 1$ as

$$\mathbf{x}_{k+1} = \{\mathbf{p}_{k+1}^n, \mathbf{v}_{k+1}^n, \mathbf{q}_{k+1}\} \tag{16}$$

where $\mathbf{x}_{k+1}$ is a 10-D vector consisting of 3-D pedestrian's position $\mathbf{p}_{k+1}^n$, 3-D velocity $\mathbf{v}_{k+1}^n$, and 4-D quaternion $\mathbf{q}_{k+1}$.

D. CKF-Based ZUPT-Aided PINS

To suppress the effect of nonlinear error in pedestrian inertial navigation, a CKF-based ZUPT-aided PINS is first formulated to estimate the position, velocity, and attitude. In general, the core process of the CKF algorithm can be briefly described in Fig. 4.

Like UKF, CKF is a cubature point Gaussian approximation filter. The main difference is the different set of sampling points for cubature point $\boldsymbol{\xi}_i$. The key step of the CKF algorithm is to convert the integration form of $\boldsymbol{\chi}_{k|k-1}^i$ to a spherical radial integration form in the calculation process. This form is used to iteratively predict the current pedestrian state based on the previous state. Then, the spherical radial criterion is used for numerical calculation. For general Gaussian integration, there
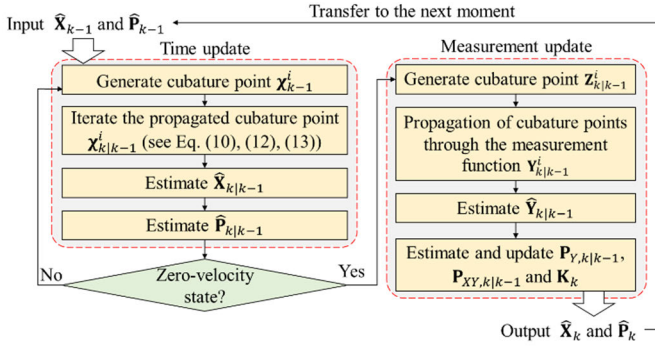
Fig. 4. Flowchart of CKF-based ZUPT-aided PINS.

is the spherical radial criterion

$$
\begin{aligned}
I_N(f) &= \int_{\mathbb{R}^N} f(x) N(x; 0, I) dx \\
&= \frac{1}{\sqrt{\pi}^n} \int f\left(\sqrt{2}x\right) \exp\left(-x^T x\right) dx \approx \sum_{i=1}^{m} \omega_i f\left(\xi_i\right)
\end{aligned}
\tag{17}
$$

where $I_N(f)$ is usually denoted as the calculating progress of system state equation and $\mathbb{R}^N$ represents the N-dimension real space over which the integration is performed. x is the differential element in the integral, which denotes the pedestrian's state to be estimated in CKF-based ZUPT-aided PINS. The cubature points ξ_i are chosen to capture the essential characteristics of the Gaussian distribution. ξ_i and corresponding weight ω_i are calculated as follows:

$$
\begin{cases}
\xi_i = \sqrt{\dfrac{m}{2}} [1]_i \\
\omega_i = \dfrac{1}{m}, \quad i = 1, \ldots, m = 2n
\end{cases}
\tag{18}
$$

where $[1]$ denotes the set of n-dimensional spatial points as the intersection of the n-dimensional unit sphere with the coordinate axes, $[1]_i$ denotes the ith column of the set, and $[1]$ is denoted as

$$
[1] = \left\{ \begin{bmatrix} 1 \\ 0 \\ \vdots \\ 0 \end{bmatrix} \begin{bmatrix} 0 \\ 1 \\ \vdots \\ 0 \end{bmatrix} \cdots \begin{bmatrix} 0 \\ 0 \\ \vdots \\ 1 \end{bmatrix} \begin{bmatrix} -1 \\ 0 \\ \vdots \\ 0 \end{bmatrix} \begin{bmatrix} 0 \\ -1 \\ \vdots \\ 0 \end{bmatrix} \cdots \begin{bmatrix} 0 \\ 0 \\ \vdots \\ -1 \end{bmatrix} \right\}.
\tag{19}
$$

1) Time Update: First, according to the covariance matrix $\mathbf{P_{k-1}}$ at the $k-1$ moment, we need to calculate the cubature point set χ_{k-1}^i as

$$
\chi_{k-1}^i = \hat{\mathbf{X}}_{k-1} + \sqrt{\mathbf{P}_{k-1}} \xi_i, \quad i = 1, 2, \ldots, m
\tag{20}
$$

where m is twice the dimension n of the equation of state and $\hat{\mathbf{X}}_{k-1}$ is the estimated state at the last moment.

Then, the cubature point set should be substituted into the system nonlinear equation f as

$$
\chi_{k|k-1}^i = f\left(\chi_{k-1}^i\right), \quad i = 0, \ldots, m
\tag{21}
$$

where f means the iterative process of the state model $\chi_{k|k-1}^i$, which can be calculated by (10)–(13). The predicted state equation $\hat{\mathbf{X}}_{k|k-1}$ can be estimated based on $\chi_{k|k-1}^i$

$$
\hat{\mathbf{X}}_{k|k-1} = \frac{1}{m} \sum_{i=1}^{2n} \chi_{k|k-1}^i.
\tag{22}
$$

Also, the predicted state covariance matrix $\hat{\mathbf{P}}_{k|k-1}$ is given by

$$
\hat{\mathbf{P}}_{k|k-1} = \frac{1}{m} \sum_{i=1}^{m} \chi_{k|k-1}^i \left(\chi_{k|k-1}^i\right)^T - \hat{\mathbf{X}}_{k|k-1}\left(\chi_{k|k-1}^i\right)^T + \mathbf{Q}_{k-1}
\tag{23}
$$

where $\mathbf{Q}_{k-1}$ is the covariance of process noise, which can be given by

$$
\mathbf{Q}_{k-1} = \left\{ \begin{matrix} [\mathbf{0}]_{3\times3} & [\mathbf{0}]_{3\times3} & [\mathbf{0}]_{3\times4} \\ [\mathbf{0}]_{3\times3} & \sigma(a)_{\tau,k-1}^{b}{}^2 \cdot \mathbf{I}_3 & [\mathbf{0}]_{3\times4} \\ [\mathbf{0}]_{4\times3} & [\mathbf{0}]_{4\times3} & \sigma(\omega)_{\tau,k-1}^{b}{}^2 \mathbf{Q}_q \mathbf{Q}_q^T \end{matrix} \right\} \cdot \Delta T
\tag{24}
$$

where $\sigma_{\tau,k-1}^a$ and $\sigma_{\tau,k-1}^\omega$ represent the standard deviation of accelerometer and gyroscope noise, respectively. $\mathbf{I}_3$ denotes a 3×3 identity matrix. $\mathbf{Q}_q$, a fundamental component in quaternion operations, can be calculated by

$$
\mathbf{Q}_q = \frac{1}{2} \begin{bmatrix} -q_2 & -q_3 & -q_4 \\ q_1 & -q_4 & -q_3 \\ q_4 & q_1 & q_2 \\ -q_3 & q_2 & q_1 \end{bmatrix}
\tag{25}
$$

where q_1–q_4 are the components of quaternion.

2) Measurement Update: Like the prediction part, we need to calculate the cubature point set $\mathbf{Z}_{k|k-1}^i$ for measurement model of system as

$$
\mathbf{Z}_{k|k-1}^i = \hat{\mathbf{X}}_{k|k-1} + \sqrt{\mathbf{P}_{k|k-1}} \xi_i, \quad i = 0, 1, \ldots, m.
\tag{26}
$$

Then, we evaluate the propagated cubature points $\hat{\mathbf{Y}}_{k|k-1}^i$ shown as

$$
\mathbf{Y}_{k|k-1}^i = \mathbf{H} \cdot \mathbf{Z}_{k|k-1}^i, \quad i = 0, 1, \ldots, m
\tag{27}
$$

where $\mathbf{H}$ is the measurement matrix denoted as

$$
\mathbf{H} = \left\{ [\mathbf{0}]_{3\times3} \quad \mathbf{I}_3 \quad [\mathbf{0}]_{3\times4} \right\}.
\tag{28}
$$

The predicted measurement matrix $\hat{\mathbf{Y}}_{k|k-1}$ can be estimated by (27) based on $\mathbf{Y}_{k|k-1}^i$

$$
\hat{\mathbf{Y}}_{k|k-1} = \frac{1}{m} \sum_{i=1}^{m} \mathbf{Y}_{k|k-1}^i.
\tag{29}
$$

Then, we can update the innovation covariance matrix $\mathbf{P}_{Y,k|k-1}$ as

$$
\mathbf{P}_{Y,k|k-1} = \frac{1}{m} \sum_{i=1}^{m} \left(\mathbf{Y}_{k|k-1}^i - \hat{\mathbf{Y}}_{k|k-1}\right) \left(\mathbf{Y}_{k|k-1}^i - \hat{\mathbf{Y}}_{k|k-1}\right)^T + \mathbf{R}_{k-1}
\tag{30}
$$

where $\mathbf{Y}_{k|k-1}^i$ is the predicted measurement at the ith cubature point and $\hat{\mathbf{Y}}_{k|k-1}$ is the mean predicted measurement. Also, $\mathbf{R}_{k-1}$ is the covariance matrix of measurement noise.

The cross-covariance matrix $\mathbf{P}_{XY,k|k-1}$ can be calculated as

$$\mathbf{P}_{XY,k|k-1} = \frac{1}{m} \sum_{i=1}^{m} \left(\mathbf{Z}_{k|k-1}^i - \hat{\mathbf{X}}_{k|k-1}\right)\left(\mathbf{Y}_{k|k-1}^i - \hat{\mathbf{Y}}_{k|k-1}^i\right)^T \tag{31}$$

where is $\mathbf{Z}_{k|k-1}^i$ the cubature point set for measurement model of system. $\hat{\mathbf{X}}_{k|k-1}$ is the predicted state equation.

Next, we can update the Kalman gain $\mathbf{K}_k$ at moment k

$$\mathbf{K}_k = \mathbf{P}_{XY,k|k-1}\left(\mathbf{P}_{Y,k|k-1}\right)^{-1}. \tag{32}$$

Finally, the pedestrians' state equation $\hat{\mathbf{X}}_k$ and the corresponding error covariance $\hat{\mathbf{P}}_k$ at moment k can be estimated

$$\hat{\mathbf{X}}_k = \hat{\mathbf{X}}_{k|k-1} + \mathbf{K}_k\left(\mathbf{Y}_k - \hat{\mathbf{Y}}_{k|k-1}\right) \tag{33}$$

$$\hat{\mathbf{P}}_k = \hat{\mathbf{P}}_{k|k-1} - \mathbf{K}_k\mathbf{P}_{Y,k|k-1}\mathbf{K}_k^T. \tag{34}$$

As suggested in Fig. 4, $\hat{\mathbf{P}}_k$ and $\hat{\mathbf{X}}_k$ will be used to estimate the pedestrian orientation as the input at the next moment. The CKF algorithm is based on the Bayesian estimation and uses the third-order spherical radial rule to calculate the target state estimates and covariances by the volume point set. This avoids the errors caused by system linearization and improves the filtering estimation accuracy. The CKF algorithm outperforms other nonlinear filtering algorithms in high-dimensional systems and applies to any form of nonlinear systems.

E. Discussion

To improve clarity and readability, we provide the detailed pseudocode for two parts at the end of this section. It is worth mentioning that the initial variable $\mathbf{X_0}$, which is required in CKF, includes the initial position, velocity, and orientation (represented by a quaternion). We assume that the IMU is static for the first few seconds, allowing us to calculate the initial roll, pitch, and yaw angles based on the average acceleration. $\mathbf{P_0}$ is determined by the uncertainty of the initial position, and the values of $\mathbf{Q_0}$ and $\mathbf{R_0}$ depend on the uncertainty of the IMU. This pseudocode is generated by LaTeX.

The proposed method maintains computational efficiency with an overall time complexity of $O(n^3)$ and space complexity of $O(n^2)$. Compared with other existing methods [31], [32], [39], [41], the proposed method remains lower computational complexity and does not have harsh memory requirements This makes it highly suitable for real-time pedestrian INSs.

IV. EXPERIMENTS AND DISCUSSION

A public PINS dataset released by the University of Toronto was first performed to verify the proposed method [50]. We also did two different real scenario experiments with a foot-mounted IMU to test its performance during complex movements, including fast and slow motion, as well as changes in direction. In this section, we will first introduce the publicly available dataset evaluation. Then, the sensor setup of our SINS will be explained in Section IV-B. Besides, we describe the two scenarios, including a long-distance promenade walk and a rectangular square we chose to evaluate the proposed method. Finally, the experiment evaluation is divided into two parts, in which the presented ZV detection and CKF-based ZUPT-aided PINS are discussed in Sections IV-D and IV-E.

Algorithm 1 Gait Interval-Aided Dual-Threshold ZV Detection

Require: *acc, gyro, w, n,* γ_1, γ_2 ▷ *w, n* are two smoothing window sizes
Ensure: *c_corrected*
1: $T1 = []$ ▷ Compute T1
2: **for** $k = w$ to $length(acc) - w$ **do**
3:    $var\_acc[k] = var(acc[k - w : k + w])$
4:    $T1_k = norm(var\_acc)$
5:    $T1.append(T1_k)$
6: **end for**
7: $T2 = []$ ▷ Compute T2
8: **for** $k = w$ to $length(gyro) - w$ **do**
9:    $T2_k = norm(gyro)$
10:   $T2.append(T2_k)$
11: **end for**
12: $c = []$ ▷ Detect ZV state
13: **for** $k = 1$ to $length(T1)$ **do**
14:   **if** $T1[k] < \gamma_1$ and $T2[k] < \gamma_2$ **then**
15:     $c.append(0)$ ▷ ZV state
16:   **else**
17:     $c.append(1)$ ▷ Motion state
18:   **end if**
19: **end for**
20: $c\_corrected = c$ ▷ Correct gait intervals
21: **for** $k = n$ to $length(c) - n$ **do**
22:   **if** $c[k] == 0$ and $\sum(c[k - n : k + n]) > n$ **then**
23:     $c\_corrected[k] = 1$
24:   **else if** $c[k] == 1$ and $\sum(c[k - n : k + n]) \le n$ **then**
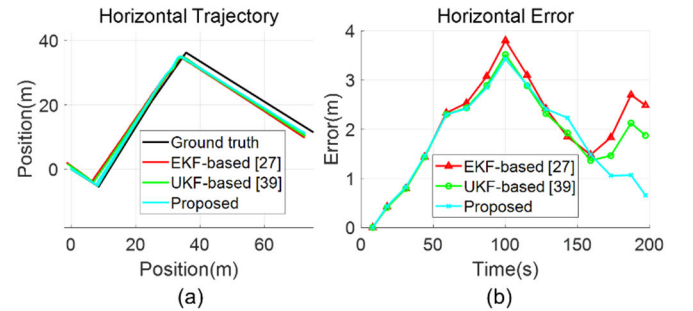25: $c\_corrected[k] = 0$
26:   **end if**
27: **end for**

Fig. 5. Evaluation result of the available dataset. (a) Trajectory generated by three methods. (b) Horizontal error compared with three methods.

A. Publicly Available Dataset Evaluation

We evaluated our proposed method using a public PINS dataset released by the University of Toronto, which can be accessed at IEEE DataPort. This dataset includes walking actions along three corridors, with an IMU sampling rate of 200 Hz and a total sampling time of 200 s. What is more, there is an intermediate vertical position ground truth for the experiment, which makes it ideal for evaluating our proposed CKF-based PINS. The results of this experiment are shown in Fig. 5.

The left plot in Fig. 5 shows the position trajectories of the ground truth, EKF-based, UKF-based, and our proposed method. We can see that while the trajectories predicted by all three methods fit well with the ground truth, our proposed

Algorithm 2 Cubature Kalman Filter-Based ZUPT-Aided PINS

Require: $\hat{\mathbf{X}}_0, \mathbf{P}_0, \mathbf{Q}_0, \mathbf{R}_0, c\_corrected$

1: **for** $k = 2$ to N **do**
2: **1) Time Update**
3:   $\chi_{k-1}^i = \hat{\mathbf{X}}_{k-1} + \sqrt{\mathbf{P}_{k-1}}\xi_i$ ▷ Generate cubature points
4:   $\chi_{k|k-1}^i = f(\chi_{k-1}^i)$
               ▷ Propagated cubature point (see Eq. (12) to (15))
5:   $\hat{\mathbf{X}}_{k|k-1} = \frac{1}{2m}\sum_{i=1}^{2m}\chi_{k|k-1}^i$ ▷ Estimate the predicted state
6:   $\mathbf{P}_{k|k-1} = \frac{1}{2m}\sum_{i=1}^{2m}(\chi_{k|k-1}^i - \hat{\mathbf{X}}_{k-1})(\chi_{k|k-1}^i - \hat{\mathbf{X}}_{k-1})^T + \mathbf{Q}_{k-1}$
               ▷ Estimate the predicted state covariance matrix
7:   **if** $c\_corrected[k] = 0$ **then**   ▷ Zero-velocity state
8:    **2) Measurement Update**
9:     $\mathbf{Z}_{k|k-1}^i = \hat{\mathbf{X}}_{k-1} + \sqrt{\mathbf{P}_{k-1}}\xi_i$ ▷ Generate cubature points
10:    $\mathbf{Y}_{k|k-1}^i = \mathbf{H} \cdot \mathbf{Z}_{k|k-1}^i$
               ▷ Propagation of cubature points through measurement
11:    $\hat{\mathbf{Y}}_{k|k-1} = \frac{1}{2m}\sum_{i=1}^{2m}\hat{\mathbf{Y}}_{k|k-1}^i$
               ▷ Estimate the predicted measurement matrix
12:    $\mathbf{P}_{Y,k|k-1} = \frac{1}{2m}\sum_{i=1}^{2m}(\hat{\mathbf{Y}}_{k|k-1}^i - \hat{\mathbf{Y}}_{k|k-1})(\hat{\mathbf{Y}}_{k|k-1}^i - \hat{\mathbf{Y}}_{k|k-1})^T + \mathbf{R}_{k-1}$
               ▷ Calculate the innovation covariance matrix
13:    $\mathbf{P}_{XY,k|k-1} = \frac{1}{2m}\sum_{i=1}^{2m}(\chi_{k|k-1}^i - \hat{\mathbf{X}}_{k|k-1})(\hat{\mathbf{Y}}_{k|k-1}^i - \hat{\mathbf{Y}}_{k|k-1})^T$
               ▷ Calculate the cross-covariance matrix
14:    $\mathbf{K}_k = \mathbf{P}_{XY,k|k-1}\mathbf{P}_{Y,k|k-1}^{-1}$ ▷ Calculate the Kalman gain
15:    $\hat{\mathbf{X}}_k = \hat{\mathbf{X}}_{k|k-1} + \mathbf{K}_k(\mathbf{Y}_k - \hat{\mathbf{Y}}_{k|k-1})$ ▷ Update the state estimate
16:    $\mathbf{P}_k = \mathbf{P}_{k|k-1} - \mathbf{K}_k\mathbf{P}_{Y,k|k-1}\mathbf{K}_k^T$ ▷ Update covariance matrix
17:   **end if**
18: **end for**

TABLE I
KEY PARAMETERS OF XSENS MTI-10 IMU

	Gyroscopes	Accelerometers
Standard full range	$\pm 450°/s$	$\pm 20g$
Initial bias error	$0.2°/s$	5mg
In-run bias stability	$18°/h$	$15\mu g$
Bandwidth (-3dB)	415Hz	375Hz
Noise density	$0.03°/s\sqrt{Hz}$	$60\mu g/\sqrt{Hz}$
Non-linearity	0.03%	0.1%

approach is closest to the ground truth. In order to show the performance of the proposed method in more detail, the comparison of the horizontal errors of the three predicted trajectories is given in the right figure. The results demonstrate that our proposed method achieves higher accuracy in position estimation compared to the other methods. The proposed method maintains lower error, particularly in scenarios where the traveling direction is opposite to the initial direction in the latter part of the experiment.

Although this experiment demonstrated the good performance of the CKF-based method, the dataset was short in duration and did not allow us to showcase the improvement provided by the nonlinearity-aware dual-threshold feature of the proposed method for ZV detection. Therefore, we conducted two follow-up field experiments to verify the method's performance when pedestrians undergo long-distance travel, direction changes, and speed variations.

B. Sensor Setups

We chose a commonly used Xsens MTi-10 IMU (Movella Inc., USA). Its dimensional specifications are $57 \times 42 \times 23.5$ mm, 52 g. The full-scale ranges of the gyroscope and accelerometer were $\pm 450°/s$ and ± 20 g. In these two experiments, we utilized the IMU to collect data for our experiments. The IMU provides accelerometer data (linear acceleration along the x-, y-, and z-axes) and gyroscope data (angular velocity around the x-, y-, and z-axes) in the body frame. The achievable max rate is 2000 Hz. Meanwhile, we utilized a sampling rate of 400 Hz in our experiments. This rate was chosen based on preliminary tests that indicated it provides a good

tradeoff between data resolution and processing efficiency. What is more, the output accelerometer and gyroscope data are the raw data instead of computing EKF at the hardware level. Key parameters describing its performance are shown in Table I.

C. Implementation of Scenarios

First, we conducted a set of long-distance walking experiments in a promenade as the first scenario for our validation. In this experiment, a pedestrian walked in a straight line about 197.43 m with the IMU mounted at the top of her foot. We used the L1 and L2 dual-frequency GNSS signals received from the u-blox ZED-F9P module for RTK solutions with 1 Hz. We regarded it as the experiment's ground truth to evaluate the proposed method's accuracy.

We also set up a set of loop closure experiments to test the performance of the proposed method in suppressing position drift. The experimenters used a foot-mounted IMU to walk around a rectangular square for one and a half loop. This aims to test whether the proposed method remains robust after the pedestrian switches walking direction. Meanwhile, as shown in Fig. 6(c), a one-and-a-half loop ensures the length of the experiment. The ground truth is derived from a LiDAR-based SLAM. The square is 61.8 m long and 36.9 m wide. The foot-mounted IMU and the experiment scenarios are shown in Fig. 6. In this experiment, we intentionally changed both the direction and the speed of walking to introduce nonlinearities in the pedestrian's motion. For example, even when the walking distance remained the same, the time taken by pedestrians differed by more than 10 s. This variation in speed and direction highlights the nonlinear characteristics of pedestrian walking. Therefore, we believe that it effectively reflects the nonlinearities in pedestrian movement.

D. Evaluation of Presented ZV Detection

To evaluate the effectiveness of the proposed ZV detection method, we utilized the proposed method to calculate the pedestrian's motion state during the long-distance experiment. We also compared our method with the conventional ZV algorithms, including MV, ARE, and GLRT, which we illustrated in Section II. During the experiment, we recorded a video of the pedestrian's movement. By carefully analyzing the video footage, we were able to manually identify and calibrate the ground truth of the ZV GIs. The results are shown in Fig. 7.
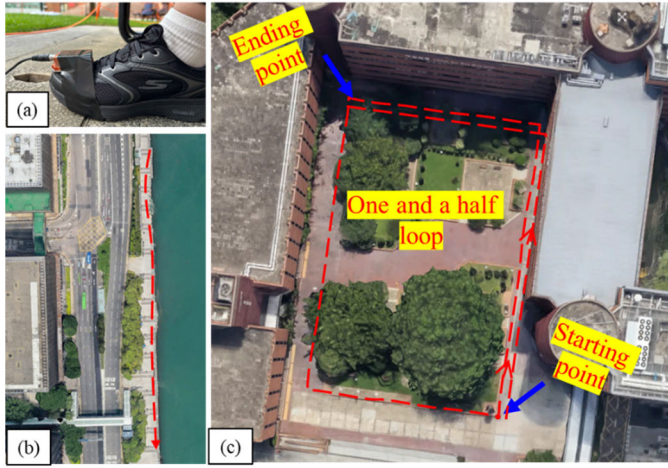
Fig. 6. (a) Foot-mounted IMU and the real-world scenarios of the two experiments. (b) Long-distance promenade. (c) Square.

TABLE II
POSITIONING ERROR COMPARISON RESULTS USING DIFFERENT
ZV DETECTION METHODS

Candidate Models	Error Category	
	Total Estimated Error[1](m)	RMSE
MV [13]	11.14	4.10
ARE [14]	55.01	24.42
No GI-aided	9.58	3.44
Proposed	**3.13**	**1.18**

[1]Total estimated length error means the difference between the predicted walk length and the ground truth.

By comparing the horizontal positioning error shown in Fig. 9, the proposed GI-aided dual-threshold ZV detection method shows competitiveness through the whole positioning process. We also listed Table II better to perform the advantage of our proposed ZV detection method.

The blue line in each figure shows the acceleration raw data during the pedestrian gait.

As for ZV detection results $\mathbf{c}'$ showed as a red line in Fig. 7, we enlarged it by a factor of 100 to change the range of values from 0 to 1–0 to 100 to allow for a better comparison with the raw data on pedestrian acceleration indicated by the blue line. The high level of the red line means that the pedestrian is moving, and the zero means that the pedestrian is in a ZV state. After iterative testing, the thresholds for all the methods were set close to the best-performing effect for better comparisons. The first row of Fig. 7 shows reference ZV with the zoomed MAG of the pedestrian's acceleration, and the next three rows show the three conventional methods, respectively. Then, the last row shows our approach's ZV detection method.

In Fig. 7, we can see that the MV and GLRT methods are more prone to detection errors in the middle of the interval, such as about the 177th and the 189th s. This is because the accelerometer values change too much and are unstable when a person is walking. The third row of Fig. 7 shows the results of the ARE method, which has more false detections and errors concentrated between the stationary/motion interval transitions. Large sudden changes in the angular velocity of the foot cause errors when it leaves and lands on the ground during walking. The last row shows that both errors are well suppressed after the biconditional joint interval determination. In particular, the interval fitting method corrects the error well at about the 177th s, even though MV and ARE give a wrong judgment.

To evaluate the contribution of our proposed GI-aided dual-threshold ZV detection to localization accuracy, Fig. 8 compares the localization results of our proposed method with MV and ARE-based ZV detections.

From the figure, we can see that the trajectories predicted by MV and ARE present serious errors. This is because the conventional ZV detections are not accurate enough to judge the motion state of pedestrians, which ultimately affects the localization accuracy. In addition, we find that the dual-threshold detection method without the GI-aided scheme performs better than those based on MV and ARE, but it is worse than the GI-aided method.

E. Evaluation of CKF Estimator in Localization

We evaluated the performance of our proposed CKF-based ZUPT-aided PINS in different scenarios compared with EKF-based and UKF-based ZUPT-aided PINS.

1) Long-Distance Promenade Experiment: Since the sampling rate of RTK localization ground truth was 1 Hz when the IMU sampling rate was 400 Hz, we downsampled the trajectories estimated by different KF-based ZUPTs to obtain the error. The localization trajectory results are shown in Fig. 10.

From Fig. 10, CKF has the highest accuracy among the three methods and predicts the most similar trajectories with the ground truth. When the pedestrian completed half of the experiment, the trajectory estimated by the EKF began to show the position drift. This is because the EKF approximates the nonlinear function by a first-order Taylor expansion when dealing with a nonlinear system, and this approximation may lead to a large prediction error when the system is highly nonlinear.

There are apparent disparities between the trajectory estimated by UKF and the ground truth after walking about 15 m. The results of UKF are not as good as expected as well, which is affected by the nonpositive nature of matrix iteration in predicting the trajectories. By adjusting the parameter κ in calculating the scaling factor, the problem of UKF's iterative failure due to matrix nonpositive definiteness can be solved, but the localization accuracy is still affected.

To analyze the effectiveness of our proposed method more precisely, we compared the positioning errors among different methods, as shown in Fig. 11.

It can be noted that the position errors of all methods present a divergent trend as there is no absolute positioning information. However, the proposed method performs the best among all methods. Table III is listed below to illustrate the positioning error comparison among different methods. By calculating the RMSE values for these models, the CKF-based ZUPT RMSE average value is lower than that of comparison models, implying that the CKF-based ZUPT is much better.

2) Loop Closure Experiment: To evaluate the accuracy of our approach in more challenging positioning scenarios with changing directions, we designed a loop closure experiment.
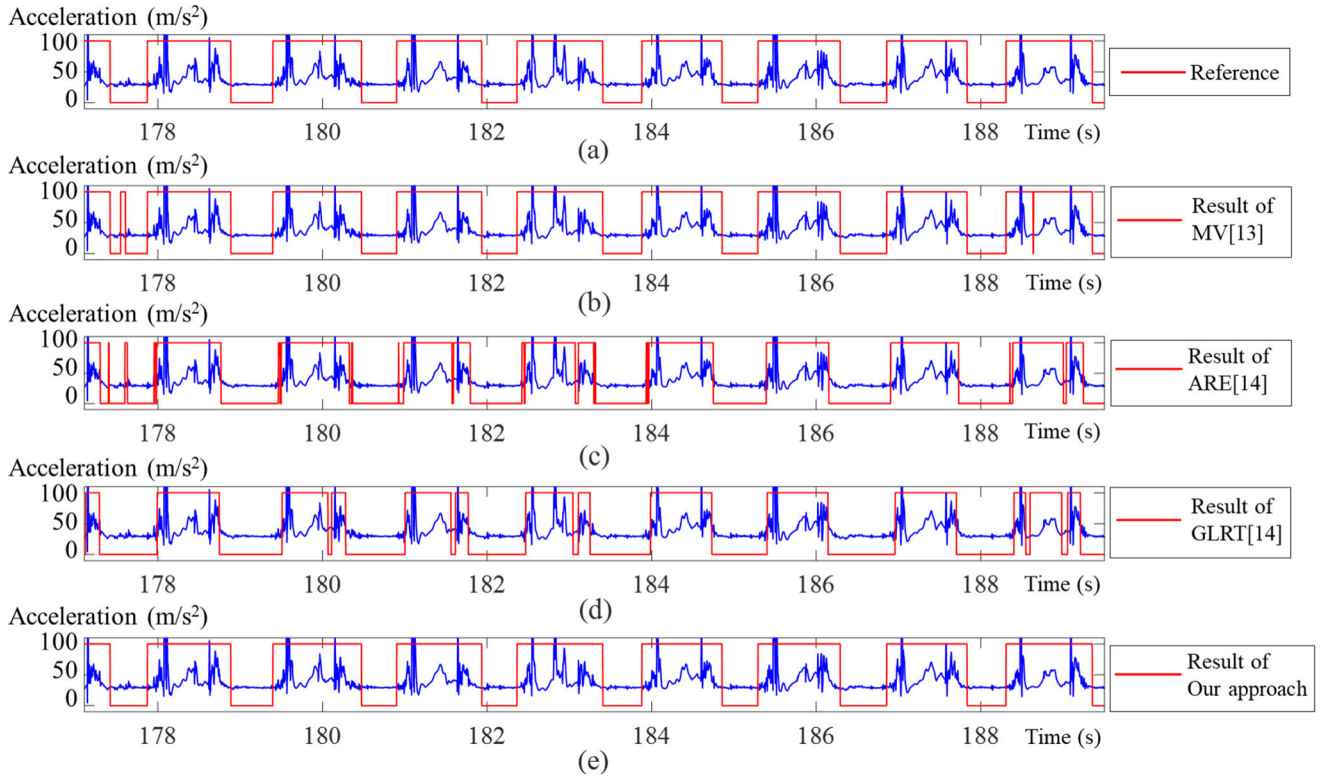
Fig. 7. Comparison between the proposed ZV detection method and three common methods. (a) Reference to the pedestrian's G. (b) Result of the acceleration MV method. (c) Result of the ARE method. (d) Result of the GLRT method. (e) Result of our proposed ZV detection method.
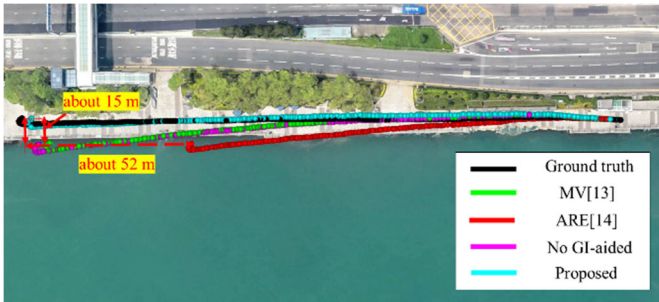

Fig. 8. Comparisons of the GI-aided dual-threshold ZV detection method with MV, ARE, and dual-threshold ZV detection without GI-aided.

TABLE III
POSITIONING ERROR COMPARISON RESULTS IN LONG-DISTANCE PROMENADE EXPERIMENT

Candidate Models	Error Category	
	Total Estimated Error[1] (m)	RMSE
EKF-based ZUPT [27]	5.22	3.69
UKF-based ZUPT [39]	7.19	25.84
Proposed	**3.17**	**1.18**

[1]Total estimated length error means the difference between the predicted walk length and the ground truth.
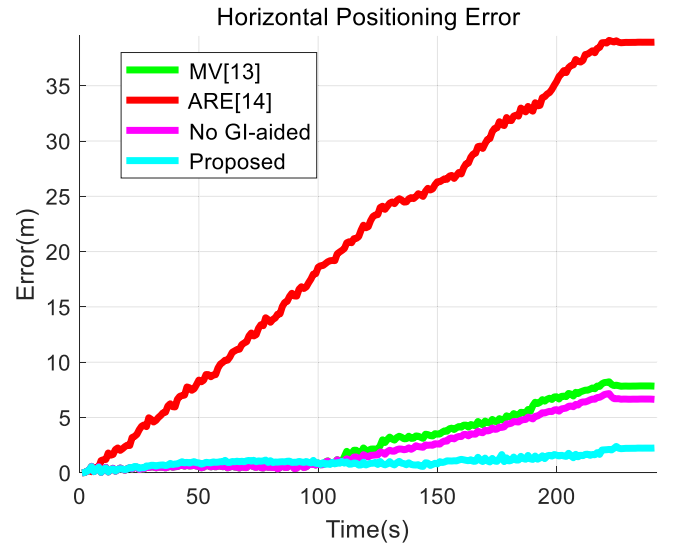

Fig. 9. Horizontal positioning error comparing the GI-aided dual-threshold ZV detection method with MV, ARE, and dual-threshold ZV detection without GI aided.

We also put the starting point and the ending point of the loop closure experiment in Fig. 12. The experiment was divided into six phases to better analyze the result in Fig. 12 too.

The trajectory comparison is shown in Fig. 13, in which the ground truth, EKF-based, UKF-based, and proposed method trajectories are represented by black, red, green, and light blue dots, respectively. From Fig. 13, it is easy to see that our proposed method is the most effective in controlling the cumulative error, followed by EKF. During the loop closure experiment, the UKF-based method also suffers from the problem of failed iteration, such as the long-distance promenade experiment caused by the negative κ parameter. It causes the covariance **P** not to remain positive definite with the iterations of KF. By manually turning up the parameter κ, we can ensure that the UKF-based method works properly. However, as seen from Fig. 13, it is not very effective and is the worst of the three methods.
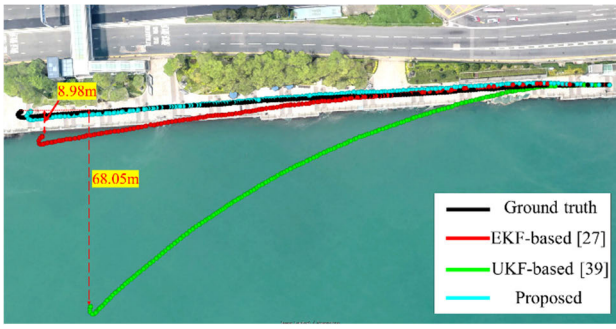
Fig. 10. Comparisons of the CKF-based method to two other commonly used KFs and ground truth.
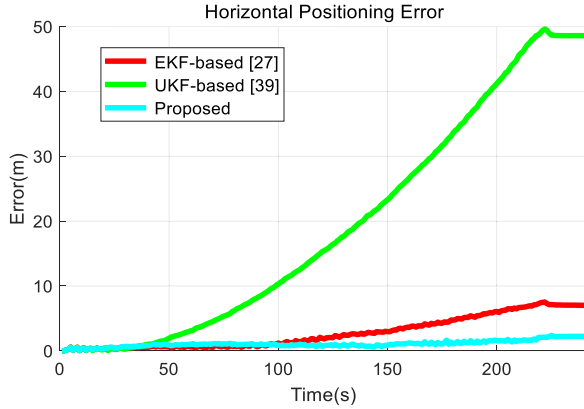

Fig. 11. Horizontal positioning error curves comparing the trajectory predicted by each method with the ground truth in ENU coordinate.
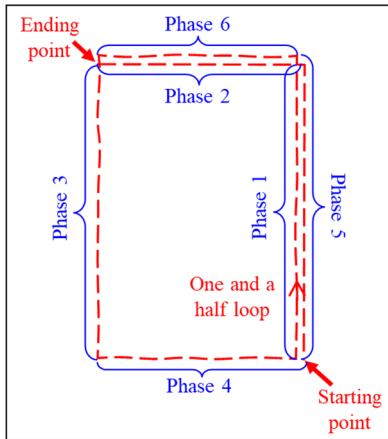

Fig. 12. Phase, starting point, and ending point of the loop closure experiment.

Fig. 13. Comparisons of the proposed method to two other commonly used KFs and ground truth.

TABLE IV
ITERATION INTERRUPTION TIMES FOR DIFFERENT VALUES OF κ

The value of κ	The time when the iteration was interrupted (s) /Total sampling time of the experiment (s)
0	83.42 / 399.48
10000	113.5 / 399.48
20000	197.85 / 399.48
25000	347.68 / 399.48

Fig. 14. Box plot comparing the horizontal positioning error for EKF-based method [27], different values of κ parameter of UKF-based method [39], and CKF-based method.

To address the impact of the κ parameter on the prediction results in the UKF, we chose a loop closure experiment to evaluate the performance of the UKF. Through repeated experiments, we found that when the value of κ is less than 27 000, the weight of the central sigma point becomes negative, causing the covariance matrix to be nonpositive definite and leading to iteration interruption. Table IV is listed to illustrate the specific circumstances of iteration termination. As the value of κ increases beyond 27 000, the covariance matrix can be properly decomposed using the Cholesky decomposition, allowing the UKF to perform trajectory prediction normally. Furthermore, the box plot comparing the horizontal positioning error for different values of κ parameter of UKF-based method
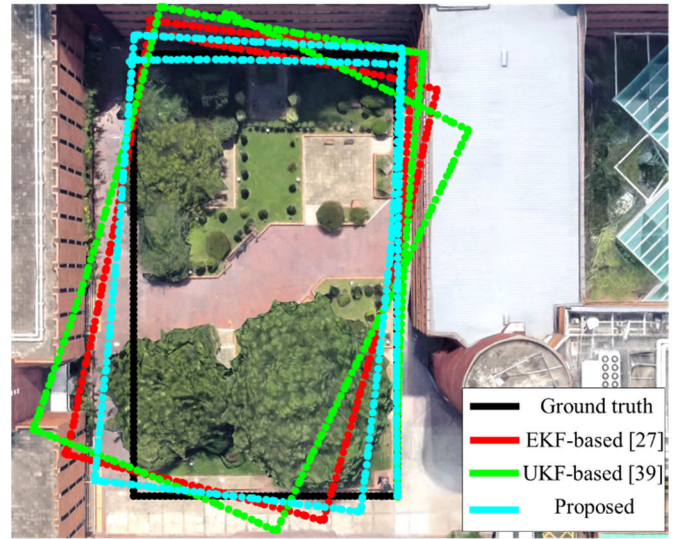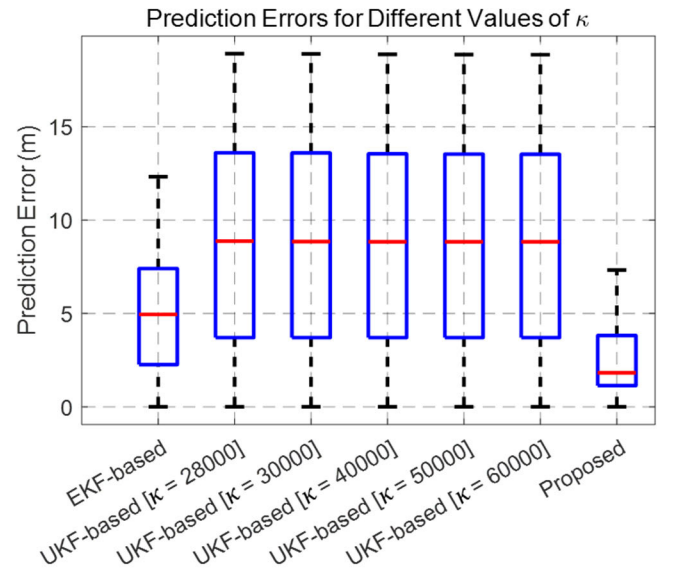
is shown in Fig. 14. We also put the box plot of EKF-based method and CKF-based method as an additional comparison. The box diagram also corroborates that the value of κ has a minimal impact on the overall trajectory prediction error when the UKF operates correctly.

We put the horizontal positioning error curves in Fig. 15. It can be noticed that the error curve for this experiment was
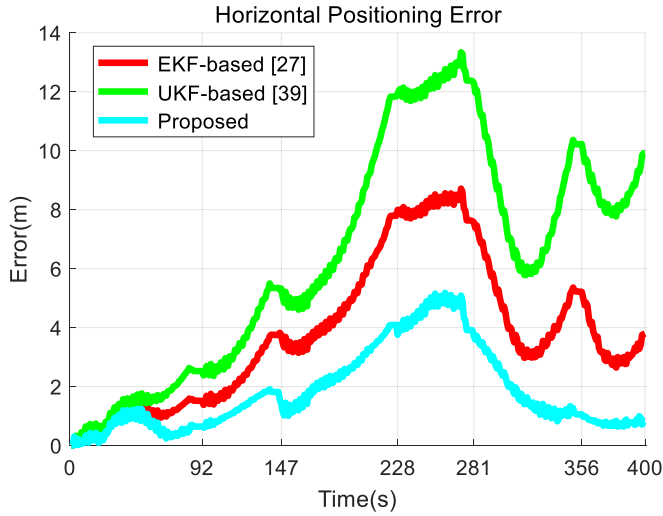
Fig. 15. Horizontal positioning error curves comparing the trajectory predicted by each method with the ground truth in the ENU coordinate.

TABLE V
POSITIONING ERROR COMPARISON RESULTS IN LOOP CLOSURE EXPERIMENT

Candidate Models	Error Category	
	Total Estimated Error[1](m)	RMSE
EKF-based ZUPT [27]	5.3436	4.5456
UKF-based ZUPT [39]	14.0616	7.5083
Proposed	**1.1816**	**2.3171**

[1]Total estimated length error means the difference between the ending point and the starting point.

Fig. 16. Time consumption curves predicted by each method.

not consistently increasing like the last long-distance experiment. The switching walking direction of the experimenter caused this difference. During phase 3 of the experiment, from 147th to 228th s in Fig. 15, the positioning error increased significantly because the experimenter's walking direction reversed from the initial direction. This highlights the challenges that the SINS model faces with the nonlinearity of human gait, as the EKF- and UKF-based methods showed abrupt increases in error, indicating their difficulty in adapting to sudden changes in direction. Conversely, the proposed method demonstrated a gentler error increase, showcasing its better handling of directional reversals.

While, in phases 5 and 6 of experiments, from 281st to 346th s and 346th to 400th s in Fig. 15, U-shaped curves appeared in the EKF and UKF-based trajectories, while CKF maintained more stable errors. This nonlinearity error arises because there are nonlinear components during the velocity and quaternion updates process of SINS. The quaternion update also assumes small angular changes, but for larger angular velocities or longer time steps, the approximation can lead to significant errors in orientation estimation. Besides, as we discussed in Section II, when the degree of nonlinearity of the system becomes stronger, the first-order Taylor series expansion step that the EKF-based method relies on will produce larger errors, leading to low estimation accuracy of the filter. The change of UKF κ parameter ensures that the iteration proceeds normally, but it still affects its prediction performance. The proposed method, however, does not exhibit a U-shaped curve during these phases because it is more accurate in judging the pedestrian's turning direction. This reflects that the proposed method has a better performance in suppressing the nonlinear error generated when pedestrians steer. Meanwhile, Table V lists the positioning error comparison among different methods. The positioning error of the proposed method remains minimized. The proposed method consistently minimized the positioning error across various phases of the experiment, demonstrating its superior ability to handle the nonlinearities of pedestrian walking more effectively than the EKF-based and UKF-based methods.

To make a comparative real-time analysis, we use the loop-closure experiment dataset to evaluate the performance of the proposed method. The result is given in Fig. 16.

The sampling rate of the IMU is 400 Hz. Our analysis shows that the proposed method has an operation time essentially on par with UKF. The running time of the proposed method is only 2 s more than that of UKF when processing 400 s of long-time data. Meanwhile, EKF-based remains the lowest operation time. If we examine the slopes of the curves, we can assess the real-time capability of each method. The slope of the operation time curve multiplied by the IMU time interval (0.0025 s) gives the time for one operation, which is less than 0.0025 s in our proposed method. It indicates that the operation can be performed in real time. We believe that this comparison curve illustrates that our proposed method is suitable for real-time applications due to its low computational overhead.

To conclude, CKF-based ZUPT-aided PINS achieves the best performance in both evaluations. In the long-distance experiment, its RMSE decreased by 67.95% and 95.42% compared to EKF and UKF, respectively. Also, in the loop closure experiment, its RMSE decreased by 49.03% and 69.04% compared to EKF and UKF, respectively.

V. CONCLUSION

This article proposes a novel nonlinearity-aware pedestrian inertial navigation based on GI-aided ZUPT and CKF. First,

we design a GI-aided dual-threshold ZV detection, which can effectively avoid interval misjudgment when complex pedestrian motions are involved, thus providing a reliable detection. Then, a CKF-based ZUPT-aided PINS is formed to achieve pedestrian positioning, which can reduce the effects of nonlinear errors, leading to improved positioning accuracy. Experiments are performed in different urban scenarios to evaluate the performance of the proposed method. The experimental results show that the method proposed can better detect the intervals of pedestrian motion and stationery. The update algorithm based on CKF performs better than conventional KF-based methods, which reduced the RMSE by 67.95% and 95.42% compared with EKF and UKF, respectively, in the long-distance experiment. In our 60×38 m loop closure experiment, its RMSE decreased by 49.03% and 69.04% compared with EKF and UKF, respectively. To sum up, we conclude that the proposed approach provides a high-precision and real-time solution for pedestrian inertial navigation.

The proposed nonlinearity-aware ZUPT-aided PINS based on CKF offers significant industrial applicability, particularly in GNSS-challenged environments requiring precise and real-time navigation solutions. This approach's high accuracy makes it highly valuable for pedestrian positioning in firefighting rescue, logistics, and supply chain management, to safeguard the personal safety of staff. In addition, the proposed approach has its potential value in wearable healthcare. It assists healthcare providers in gaining a more comprehensive understanding of a patient's leg rehabilitation by providing more accurate gait analysis and activity prediction, thus better tailoring the treatment plan for the patient.

For future work, we plan to integrate high-definition maps (HD maps) and Wi-Fi round-trip time (RTT) technology. These technologies can provide absolute positioning information and complement the proposed method. They can help achieve more stable and accurate positioning results, especially in positioning scenarios lasting more than half an hour, where the accumulating errors generated by this approach still impact accuracy. The HD maps will offer detailed environmental context, while Wi-Fi RTT can provide precise distance measurements from known anchor points, thereby mitigating the drift errors inherent in IMU-based systems. By combining these absolute positioning techniques with our proposed method, we aim to develop a robust hybrid system capable of delivering highly accurate and reliable positioning overextended periods, suitable for a wide range of industrial applications.

REFERENCES

[1] D. Wang, Y. Dong, Z. Li, Q. Li, and J. Wu, "Constrained MEMS-based GNSS/INS tightly coupled system with robust Kalman filter for accurate land vehicular navigation," *IEEE Trans. Instrum. Meas.*, vol. 69, no. 7, pp. 5138–5148, Jul. 2020.

[2] L.-T. Hsu, Y. Gu, and S. Kamijo, "Sensor integration of 3D map aided GNSS and smartphone PDR in urban canyon with dense foliage," in *Proc. IEEE/ION Position, Location Navigat. Symp. (PLANS)*, Apr. 2016, pp. 85–90.

[3] X. Wang, X. Li, H. Chang, S. Li, Z. Shen, and Y. Zhou, "GIVE: A tightly coupled RTK-inertial–visual state estimator for robust and precise positioning," *IEEE Trans. Instrum. Meas.*, vol. 72, pp. 1–15, 2023.

[4] X. Li, Y. Yuan, X. Han, X. Li, and Y. Fu, "Toward wide-area and high-precision positioning with LEO constellation augmented PPP-RTK," *IEEE Trans. Instrum. Meas.*, vol. 73, pp. 1–13, 2024.

[5] W. W. Wen and L.-T. Hsu, "3D LiDAR aided GNSS NLOS mitigation in urban canyons," *IEEE Trans. Intell. Transp. Syst.*, vol. 23, no. 10, pp. 18224–18236, Oct. 2022.

[6] P. D. Groves and Z. Jiang, "Height aiding, C/N0 weighting and consistency checking for GNSS NLOS and multipath mitigation in urban areas," *J. Navigat.*, vol. 66, no. 5, pp. 653–669, Sep. 2013.

[7] P. Lyu, B. Wang, J. Lai, S. Bai, M. Liu, and W. Yu, "A factor graph optimization method for high-precision IMU based navigation system," *IEEE Trans. Instrum. Meas.*, vol. 1, pp. 1–19, 2023.

[8] M. Sun, Y. Wang, W. Joseph, and D. Plets, "Indoor localization using mind evolutionary algorithm-based geomagnetic positioning and smartphone IMU sensors," *IEEE Sensors J.*, vol. 22, no. 7, pp. 7130–7141, Apr. 2022.

[9] O. J. Woodman, *An Introduction to Inertial Navigation*. Cambridge, U.K.: Cambridge Univ. Press, 2007.

[10] A. Noureldin, T. B. Karamat, M. D. Eberts, and A. El-Shafie, "Performance enhancement of MEMS-based INS/GPS integration for low-cost navigation applications," *IEEE Trans. Veh. Technol.*, vol. 58, no. 3, pp. 1077–1096, Mar. 2009.

[11] J. W. Kim, H. J. Jang, D.-H. Hwang, and C. Park, "A step, stride and heading determination for the pedestrian navigation system," *J. Global Positioning Syst.*, vol. 3, no. 1, pp. 273–279, Dec. 2004.

[12] Z. Wang, H. Zhao, S. Qiu, and Q. Gao, "Stance-phase detection for ZUPT-aided foot-mounted pedestrian navigation system," *IEEE/ASME Trans. Mechatronics*, vol. 20, no. 6, pp. 3170–3181, Dec. 2015.

[13] I. Skog, J.-O. Nilsson, and P. Handel, "An open-source multi inertial measurement unit (MIMU) platform," in *Proc. Int. Symp. Inertial Sensors Syst. (ISISS)*, Feb. 2014, pp. 1–4.

[14] I. Skog, J.-O. Nilsson, and P. Handel, "Evaluation of zero-velocity detectors for foot-mounted inertial navigation systems," in *Proc. Int. Conf. Indoor Position. Indoor Navigat. (IPIN)*, Sep. 2010, pp. 1–6.

[15] W. Yang, C. Xiu, J. Zhang, and D. Yang, "A novel 3D pedestrian navigation method for a multiple sensors-based foot-mounted inertial system," *Sensors*, vol. 17, no. 11, p. 2695, Nov. 2017.

[16] K. Ryu, J. Kang, and D. Lee, "Performance comparison between EKF and UKF in GPS/INS low observability conditions," in *Proc. 21st Int. Conf. Control Autom. Syst. (ICCAS)*, 2021, pp. 1911–1916.

[17] J. Zarei and E. Shokri, "Convergence analysis of non-linear filtering based on cubature Kalman filter," *IET Sci., Meas. Technol.*, vol. 9, no. 3, pp. 294–305, May 2015.

[18] R. Xu and W. Wen. *PINS-Dataset*. Accessed: Dec. 1, 2024. [Online]. Available: https://github.com/RuijieXu0408/PINS-datasets-based-on-Xsens-IMU

[19] X. Tao, F. Zhu, X. Hu, W. Liu, and X. Zhang, "An enhanced foot-mounted PDR method with adaptive ZUPT and multi-sensors fusion for seamless pedestrian navigation," *GPS Solutions*, vol. 26, no. 1, pp. 1–13, Jan. 2022.

[20] A. Ferrari, P. Ginis, M. Hardegger, F. Casamassima, L. Rocchi, and L. Chiari, "A mobile Kalman-filter based solution for the real-time estimation of spatio-temporal gait parameters," *IEEE Trans. Neural Syst. Rehabil. Eng.*, vol. 24, no. 7, pp. 764–773, Jul. 2016.

[21] W. Kang and Y. Han, "SmartPDR: Smartphone-based pedestrian dead reckoning for indoor localization," *IEEE Sensors J.*, vol. 15, no. 5, pp. 2906–2916, May 2015.

[22] S. Beauregard and M. Klepal, "Indoor PDR performance enhancement using minimal map information and particle filters," in *Proc. IEEE/ION Position, Location Navigat. Symp.*, May 2008, pp. 141–147.

[23] M. Ji, X. Xu, and Y. Guo, "An adaptive heading correction algorithm for suppressing magnetic interference in inertial navigation system," *IEEE Trans. Instrum. Meas.*, vol. 70, pp. 1–10, 2021.

[24] T. Zhao and M. J. Ahamed, "Pseudo-zero velocity re-detection double threshold zero-velocity update (ZUPT) for inertial sensor-based pedestrian navigation," *IEEE Sensors J.*, vol. 21, no. 12, pp. 13772–13785, Jun. 2021.

[25] I. I. Mueller, "Inertial survey systems in the geodetic arsenal," *J. Geodesy*, vol. 55, no. 4, pp. 272–285, Dec. 1981.

[26] J. F. Wagner, M. Kohl, and B. Györfi, "Reevaluation of algorithmic basics for ZUPT-based pedestrian navigation," *IEEE Access*, vol. 10, pp. 118419–118437, 2022.

[27] E. Foxlin, "Pedestrian tracking with shoe-mounted inertial sensors," *IEEE Comput. Graph. Appl.*, vol. 25, no. 6, pp. 38–46, Nov. 2005.

[28] H. L. Van Trees, *Detection, Estimation, and Modulation Theory, Part I: Detection, Estimation, and Linear Modulation Theory*. Hoboken, NJ, USA: Wiley, 2004.

[29] H. Li et al., "Adaptive threshold based ZUPT for single IMU enabled wearable pedestrian localization," *IEEE Internet Things J.*, vol. 1, no. 1, pp. 1–19, Apr. 2023.

[30] S. Y. Cho and C. G. Park, "Threshold-less zero-velocity detection algorithm for pedestrian dead reckoning," in *Proc. Eur. Navigat. Conf. (ENC)*, Apr. 2019, pp. 1–5.

[31] X. Yu et al., "AZUPT: Adaptive zero velocity update based on neural networks for pedestrian tracking," in *Proc. IEEE Global Commun. Conf.*, May 2019, pp. 1–6.

[32] Z. Wang, Z. Xiong, L. Xing, Y. Ding, and Y. Sun, "A method for autonomous multi-motion modes recognition and navigation optimization for indoor pedestrian," *Sensors*, vol. 22, no. 13, p. 5022, Jul. 2022.

[33] A. R. J. Jiménez Ruiz, F. Seco Granja, J. Carlos Prieto Honorato, and J. I. Guevara Rosas, "Pedestrian indoor navigation by aiding a foot-mounted IMU with RFID signal strength measurements," in *Proc. Int. Conf. Indoor Positioning Indoor Navigat.*, Sep. 2010, pp. 1–7.

[34] Y. Zhang, X. Tan, and C. Zhao, "UWB/INS integrated pedestrian positioning for robust indoor environments," *IEEE Sensors J.*, vol. 20, no. 23, pp. 14401–14409, Dec. 2020.

[35] L. Qi et al., "A robust foot-mounted positioning system based on dual IMU data and ultrasonic ranging," *IEEE Sensors J.*, vol. 23, no. 4, pp. 4085–4095, Feb. 2023.

[36] W. Qiuying, G. Zheng, Z. Minghui, C. Xufei, W. Hui, and J. Li, "Research on pedestrian location based on dual MIMU/magnetometer/ultrasonic module," in *Proc. IEEE/ION Position, Location Navigat. Symp. (PLANS)*, Apr. 2018, pp. 565–570.

[37] G. Welch and G. Bishop, *An Introduction to the Kalman Filter*. Chapel Hill, NC, USA: Univ. of North Carolina at Chapel Hill, 1995.

[38] X. Zhang, S. Dai, H. Dai, W. Quau, and Y. Zhao, "An improved Bayesian zero-velocity detection algorithm for pedestrian navigation based on MIMU," in *Proc. 33rd Chin. Control Decis. Conf. (CCDC)*, May 2021, pp. 3418–3422.

[39] S. J. Julier and J. K. Uhlmann, "Unscented filtering and nonlinear estimation," *Proc. IEEE*, vol. 92, no. 3, pp. 401–422, Mar. 2004.

[40] S. Du, Y. Huang, B. Lin, J. Qian, and Y. Zhang, "A lie group manifold-based nonlinear estimation algorithm and its application to low-accuracy SINS/GNSS integrated navigation," *IEEE Trans. Instrum. Meas.*, vol. 71, pp. 1–27, 2022.

[41] N. Hajati and A. Rezaeizadeh, "A wearable pedestrian localization and gait identification system using Kalman filtered inertial data," *IEEE Trans. Instrum. Meas.*, vol. 70, pp. 1–8, 2021.

[42] R. V. Garcia, P. C. P. M. Pardal, H. K. Kuga, and M. C. Zanardi, "Nonlinear filtering for sequential spacecraft attitude estimation with real data: Cubature Kalman filter, unscented Kalman filter and extended Kalman filter," *Adv. Space Res.*, vol. 63, no. 2, pp. 1038–1050, Jan. 2019.

[43] I. Arasaratnam and S. Haykin, "Cubature Kalman filters," *IEEE Trans. Autom. Control*, vol. 54, no. 6, pp. 1254–1269, Jun. 2009.

[44] W. Guangcai, X. Xu, and T. Zhang, "MM estimation-based robust cubature Kalman filter for INS/GPS integrated navigation system," *IEEE Trans. Instrum. Meas.*, vol. 70, pp. 1–11, 2021.

[45] Y. Wang, Z. Yang, Y. Wang, Z. Li, V. Dinavahi, and J. Liang, "Resilient dynamic state estimation for power system using cauchy-kernel-based maximum correntropy cubature Kalman filter," *IEEE Trans. Instrum. Meas.*, vol. 72, pp. 1–11, 2023.

[46] J. Enayati, A. Rahimnejad, L. Vanfretti, S. A. Gadsden, and M. Al-Shabi, "Dynamic harmonic estimation using a novel robust filtering strategy: Iterated sliding innovation cubature filter," *IEEE Trans. Instrum. Meas.*, vol. 72, pp. 1–10, 2023.

[47] Z.-Q. Zhang and X. Meng, "Use of an inertial/magnetic sensor module for pedestrian tracking during normal walking," *IEEE Trans. Instrum. Meas.*, vol. 64, no. 3, pp. 776–783, Mar. 2015.

[48] A. R. Anwary, H. Yu, and M. Vassallo, "Optimal foot location for placing wearable IMU sensors and automatic feature extraction for gait analysis," *IEEE Sensors J.*, vol. 18, no. 6, pp. 2555–2567, Mar. 2018.

[49] T. Gujarathi and K. Bhole, "Gait analysis using imu sensor," in *Proc. 10th Int. Conf. Comput., Commun. Netw. Technol. (ICCCNT)*, Jul. 2019, pp. 1–5.

[50] B. Wagstaff, V. Peretroukhin, and J. Kelly, "Robust data-driven zero-velocity detection for foot-mounted inertial navigation," *IEEE Sensors J.*, vol. 20, no. 2, pp. 957–967, Jan. 2020.

Ruijie Xu was born in Ganzhou, Jiangxi, China. She received the B.E. degree in communication engineering from Beijing University of Chemical Technology, Beijing, China, in 2023. She is currently pursuing the M.Phil. degree in aeronautical and aviation engineering from The Hong Kong Polytechnic University, Hong Kong.

Her research interests include pedestrian inertial navigation systems, collaborative SLAM, and hardware–software co-design.

Shichao Chen (Member, IEEE) received the M.S. degree in control theory and control engineering from the School of Technology, Beijing Forestry University, Beijing, China, in 2013, and the Ph.D. degree in computer technology and application from the Faculty of Information Technology, Macau University of Science and Technology, Macau, China, in 2021.

Now, he is an Associate Professor with the State Key Laboratory of Multimodal Artificial Intelligence Systems, Institute of Automation, Chinese Academy of Sciences, Beijing. His research interests include edge computing, industrial internet, and robotics.

Dr. Chen won the Outstanding Automation Engineer Award of Chinese Association of Automation (CAA) in 2019.

Shiyu Bai (Member, IEEE) was born in Xuzhou, Jiangsu, China. He received the Ph.D. degree in navigation, guidance, and control from Nanjing University of Aeronautics and Astronautics, Nanjing, China, in 2022.

He is currently a Post-Doctoral Fellow at the Department of Aeronautical and Aviation Engineering, The Hong Kong Polytechnic University, Hong Kong. His research interests include inertial navigation, multisensor fusion, and indoor and vehicular positioning.

Weisong Wen (Member, IEEE) received the B.Eng. degree in mechanical engineering from Beijing Information Science and Technology University (BISTU), Beijing, China, in 2015, the M.Eng. degree in mechanical engineering from China Agricultural University, Beijing, in 2017, and the Ph.D. degree in mechanical engineering from The Hong Kong Polytechnic University (PolyU), Hong Kong, in 2020.

He was a Visiting Ph.D. Student with the Faculty of Engineering, University of California, Berkeley, CA, USA, in 2018. Before joining PolyU as an Assistant Professor in 2023, he was a Research Assistant Professor at AAE, PolyU, since 2021. His research interests include trustworthy multisensory integration, LiDAR SLAM, GNSS positioning, and autonomous systems.